Electro-osmotic flow enhancement over superhydrophobic surfaces

Sebastian Dehe,[1,*] Baruch Rofman,[2,*] Moran Bercovici,[2,3,†] and Steffen Hardt[1,‡]
[1]*Department of Mechanical Engineering, Technische Universität Darmstadt, 64287 Darmstadt, Germany*
[2]*Faculty of Mechanical Engineering, Technion–Israel Institute of Technology, Haifa 3200003, Israel*
[3]*Department of Mechanical Engineering, The University of Texas at Austin, Austin, Texas 78712, USA*

(Received 15 August 2019; accepted 14 April 2020; published 15 May 2020)

Electro-osmotic flow is a well-established and efficient method for driving microchannel flows that relies on the interaction of an externally applied electric field with charge arising at the interface between the liquid and the channel walls. However, its relatively low velocities together with its dependence on the *p*H of the liquid severely limit its utility. Here we experimentally demonstrate fast electro-osmotic flow over microstructured superhydrophobic surfaces. By suspending the electrolyte in a Cassie-Baxter state over hierarchical surfaces, we create stable gas-liquid interfaces on which we induce charge through a gate electrode. We provide a detailed investigation and characterization of the electro-osmotic velocity as a function of the surface geometry by utilizing particle tracking velocimetry in a microfluidic device and show that the resulting electro-osmotic velocity scales with the ratio of slip length to double-layer thickness. Compared to no-slip surfaces, we demonstrate an order of magnitude enhancement in velocity and complete *p*H independence, enabling wider utility of electro-osmotic flow in manipulation of microscale flows.

DOI: 10.1103/PhysRevFluids.5.053701

I. INTRODUCTION

Electro-osmotic flow (EOF) is the fluid motion due to the interaction of an external electric field with charges in the electric double layer (EDL), usually formed at solid-liquid interfaces due to a chemical reaction of the liquid with the solid surface. Predictions for EOF velocity were traditionally all based on a no-slip assumption at the wall, in good agreement with experimental observations [1–5]. Melcher and Taylor reported that EOF can also be obtained at naturally uncharged gas-liquid interfaces, by capacitively inducing charge using an electrode in the gas phase [6]. In the context of the rapid development of microfluidics over the past 25 years, the classic no-slip boundary condition at solid-liquid interfaces was revisited, unveiling a number of interesting phenomena [7–12]. For example, at homogeneously charged hydrophobic surfaces exhibiting molecular slip, EOF enhancement factors of the order of $1 + \beta/\lambda_D$ were predicted, where β is the slip length and λ_D the Debye length [13–15]. This idea was generalized by Ajdari and Bocquet [16] to several surface-driven transport mechanisms, and a corresponding EOF flow enhancement was indeed observed experimentally by Bouzigues *et al.* in the range of $1 + \beta/\lambda_D \approx 2$ [17]. For heterogeneous interfaces exhibiting alternating slip and no-slip patterns, Squires derived a generalization of the

*These authors contributed equally to this work.
†Corresponding author: mberco@technion.ac.il
‡Corresponding author: hardt@nmf.tu-darmstadt.de

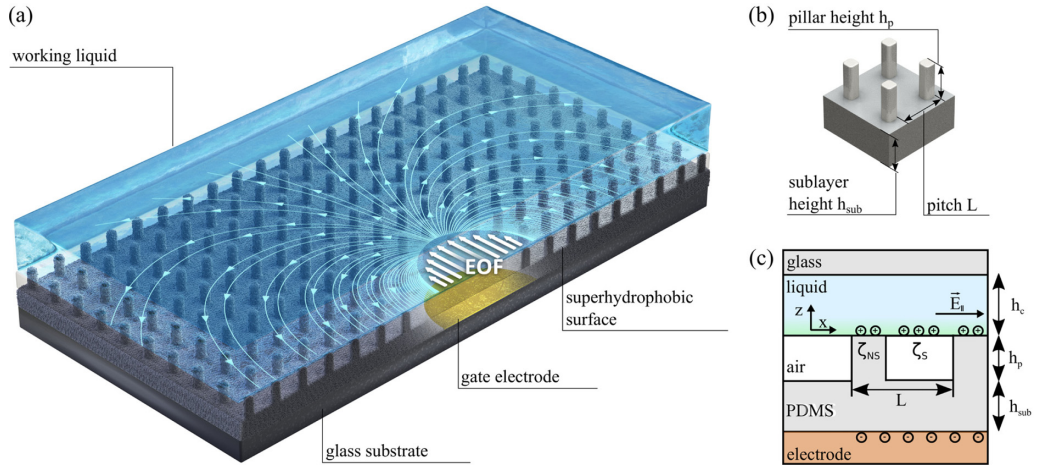

FIG. 1. Electro-osmotic flow over superhydrophobic surfaces. (a) An aqueous electrolyte is suspended over a superhydrophobic surface, enclosing air in between the surface features. Via a gate electrode, charge is induced at the gas-liquid interface, which is exposed to a driving electric field, leading to fluid motion. (b) Schematic of the microstructured superhydrophobic surface with the corresponding geometric parameters. (c) Schematic of the different layers of the configuration. The gate electrode induces charge inside the liquid, expressed by the surface potentials ζ_S and ζ_{NS}.

Helmholtz-Smoluchowski equation [18]

$$\vec{u}_{\mathrm{EOF}} = -\frac{\epsilon \vec{E}}{\eta}\left(\zeta_{\mathrm{NS}} + \zeta_{\mathrm{S}}\frac{\beta}{\lambda_D}\right). \tag{1}$$

Here ϵ represents the electric permittivity of the fluid, $\vec{E}$ is the external electric field, η is the dynamic viscosity of the fluid, and ζ_S and ζ_{NS} are the surface potentials at the slip and no-slip interfaces, respectively.

Since superhydrophobic surfaces (SHSs) that are based on microstructures and for which the liquid is in a Cassie-Baxter state exhibit large effective slip lengths [19–24], large flow enhancement factors of the order of 10^3 or higher can be expected for homogeneously charged surfaces [25,26]. However, in practice, no significant net charge exists at the gas-liquid interface [27]. Various efforts have been reported to locally control the surface charge using gate electrodes [28–31], e.g., in the context of field-effect flow control on solid surfaces [32–36]. Hardt and co-workers, following the work of Melcher and Taylor, suggested the use of a gate electrode below a superhydrophobic surface to induce charge at the gas-liquid interface and predicted an orders-of-magnitude flow enhancement relative to EOF due to native ζ potentials [37,38]. However, experimental work demonstrating EOF enhancement over superhydrophobic surfaces is lacking.

In this work, we present an experimental demonstration of electro-osmotic flow enhancement over superhydrophobic surfaces using gate electrodes. As illustrated in Fig. 1, we utilize a hierarchical surface composed of micropillars coated by nanoparticles to maintain the liquid in a Cassie-Baxter state, thus entrapping air in between the microstructures. We use a gate electrode embedded in the surface to induce charge at the gas-liquid interface and drive the flow inside a microfluidic chamber. By modifying the pitch L of the pillars [see Figs. 1(b) and 1(c)], we explore the dependence of the velocity on the slip length of the surfaces, confirming the theoretical β/λ_D dependence. For surfaces with large slip [$\beta = O(1\text{–}25\ \mu\mathrm{m})$] we obtain a velocity enhancement of one order of magnitude relative to nonslipping surfaces. In contrast to flat surfaces, over which EOF is highly sensitive to pH, we show that in our experiments it is essentially independent of pH.

II. FLOW CHARACTERIZATION

A. Theoretical modeling

For flat surfaces, a framework for shaping flow in a Hele-Shaw setup with a nonuniform ζ potential distribution has been developed [39–41]. We adapt the height-averaged theory by varying the interfacial boundary condition to implement an effective slip length, as demonstrated, for example, by Schönecker and Hardt [38]. Despite not having explicit information about their z position, observing the two-dimensional particle motion, in conjunction with the appropriate height-averaged theory, our setup provides a simple yet effective tool to evaluate the flow enhancement over superhydrophobic surfaces. In the limit of isotropic [42], perfectly slipping gas-liquid interfaces (i.e., the viscous stresses due to the gas are neglected), the boundary condition at the SHS can be modeled as

$$\vec{u}_\parallel|_{z=0\ \mu\mathrm{m}} = -\frac{\epsilon \vec{E}_\parallel}{\eta}\left(\zeta_{\mathrm{NS}} + \zeta_{\mathrm{S}}\frac{\beta}{\lambda_D}\right) + \beta\left.\frac{\partial \vec{u}_\parallel}{\partial z}\right|_{z=0\ \mu\mathrm{m}}, \tag{2}$$

where the symbol $\parallel$ denotes the projection onto the xy plane [see Fig. 1(c) for parameter definitions].

A detailed derivation of the governing equations is provided in Appendix A. Briefly, we follow the derivation by Boyko *et al.* [39] and implement Eq. (2) as the boundary condition at the lower wall. Defining $\langle \vec{u}_\parallel \rangle$ as the depth averaged velocity and ψ as the corresponding stream function satisfying $\langle \vec{u}_\parallel \rangle = (\partial\psi/\partial y, -\partial\psi/\partial x)$, the governing equations can be expressed as

$$\nabla_\parallel^2 p = 12\frac{\epsilon}{h_c^2}\vec{E}_\parallel \cdot \vec{\nabla}_\parallel \langle\zeta\rangle_{\mathrm{SHS}}, \tag{3a}$$

$$\nabla_\parallel^2 \psi_{\mathrm{SHS}} = \left(\frac{\epsilon}{\eta}\vec{E}_\parallel \times \vec{\nabla}_\parallel \langle\zeta\rangle_{\mathrm{SHS}}\right)\cdot \vec{e}_z. \tag{3b}$$

Here $\vec{e}_z$ is the unit vector in the z direction and the stream function ψ_{SHS} and the height-averaged potential $\langle\zeta\rangle_{\mathrm{SHS}}$ are defined through

$$\psi_{\mathrm{SHS}} = \frac{1+\beta/h_c}{1+4\beta/h_c}\psi, \tag{4a}$$

$$\langle\zeta\rangle_{\mathrm{SHS}} = \frac{(1+2\beta/h_c)\zeta_{\mathrm{U}} + \zeta_{\mathrm{NS}} + \frac{\beta}{\lambda_D}\zeta_{\mathrm{S}}}{2(1+4\beta/h_c)}. \tag{4b}$$

Equation (4b) introduces an effective surface potential, and in the limit of no-slip surfaces, the arithmetic average $\langle\zeta\rangle = 1/2(\zeta_{\mathrm{U}} + \zeta_{\mathrm{NS}})$ is obtained.

In the case of a disk-shaped electrode of radius r_0, when inducing an effective potential $\langle\zeta_0\rangle$ subjected to an in-plane electric field $\vec{E}_\parallel = (E_0, 0)$, the solution of Eqs. (3a) and (3b) is a dipole flow field in the outer region of the disk, with a uniform velocity in the inner region [39]. For the case of a superhydrophobic surface, the velocity magnitude is

$$\langle u_\parallel\rangle_{\mathrm{in}} = -\frac{1}{4}\frac{1}{1+\beta/h_{\mathrm{c}}}\frac{\epsilon E_0}{\eta}\left(\zeta_{\mathrm{NS}}^{\mathrm{ind}} + \zeta_{\mathrm{S}}^{\mathrm{ind}}\frac{\beta}{\lambda_D}\right), \tag{5}$$

which will serve as the theoretical benchmark for the experiments.

B. Experimental setup

Figure 2(a) presents a schematic of the experimental setup which consists of a structured surface serving as the floor of a 2 cm × 1 cm × 100 μm (length × width × depth) Hele-Shaw cell. Figure 2(b) shows a scanning electron microscopy image of a typical micropillared superhydrophobic surface used in the experiments. All of the pillars have a $5 \times 5\ \mu\mathrm{m}^2$ base cross section and are produced by standard soft lithography from polydimethylsiloxane (PDMS). In order to enhance the stability of the Cassie-Baxter wetting state, we coat the surface with a secondary nanostructure

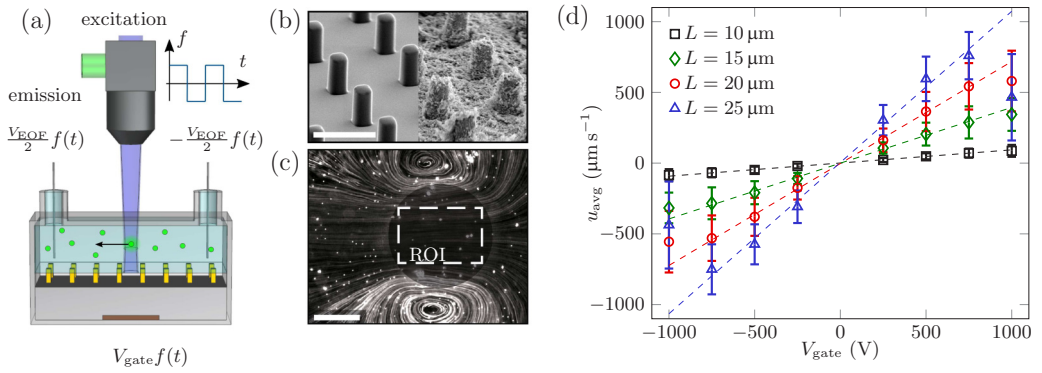

FIG. 2. Measurements of EOF over superhydrophobic surfaces. (a) The experimental configuration consists of an aqueous solution suspended in a Cassie-Baxter state over a superhydrophobic surface. A gate electrode induces charge at the gas-liquid interface in a time-periodic manner, synchronized with an externally applied field parallel to the surface, resulting in EOF. (b) Stitched scanning electron microscopy image of a typical superhydrophobic surface used in the experiments. The PDMS surface consists of an array of micropillars, coated with PVC nanoparticles (left, before coating; right, after coating). The scale bar represents 20 μm. (c) Fluorescence image showing the velocity streaklines resulting from EOF induced by the circular electrode. The reported velocity values are obtained by ensemble averaging over the central region of the circular electrode (indicated by ROI). The scale bar represents 200 μm. (d) Experimental results showing the depth-averaged velocities over superhydrophobic surfaces with different pillar spacing. The velocities are recorded over 1 min for a driving field of 50 V/cm and an AC frequency of 5 Hz with a buffer solution at an ionic strength of 10 mM at a pH of 7. The error bars represent 95%-confidence intervals based on at least six independent measurements. The dashed lines represent linear fits for the range from −750 to 750 V.

made of polyvinyl chloride (PVC) [43]. For details on the fabrication of the surfaces and channel, see Appendix B. In order to study the influence of effective slip length variations, we employ pillar pitches of $L = 10$, 15, 20, and 25 μm [see Table I for values of the geometric parameters shown in Fig. 1(c)]. The PDMS layer is placed on top of a glass slide containing a microfabricated disk-shaped gate electrode (diameter $d_{disk} = 500$ μm) used to induce charge at the gas-liquid interface.

We apply the driving electric field through two platinum wire electrodes immersed into the reservoirs at each side of the cell and connected to a multichannel power source (Labsmith HVS448-6000D) that also provides the potential for the gate electrode. In order to induce flow above the electrode, we utilize a time-periodic driving voltage of alternating sign and zero mean (rectangular signal with a frequency of 5 Hz) such that the fluid motion due to the native ζ potential

TABLE I. Geometric parameters of the pillared surfaces. The parameters are defined in Fig. 1(b).

Pillar pitch L (μm)	Pillar height h_p (μm)	Sublayer height h_{sub} (μm)	Solid fraction without PVC ϕ	Solid fraction with PVC[a] ϕ_{PVC}	Effective slip length[b] β (μm)
5	10	130	0.2500	0.3318	1.15
10	15	120	0.1111	0.1475	5.74
15	15	120	0.0625	0.0830	13.01
20	15	120	0.0400	0.0531	22.95

[a]Based on pillar shape with PVC on the sidewalls. The shape is approximated from SEM images, indicating a circular shape with diameter $d = 6.5$ μm.
[b]Obtained from Ref. [47] based on ϕ_{PVC}.

averages to zero. By simultaneously applying a synchronized AC signal at the gate electrode with amplitude V_{gate}, a nonzero time-averaged fluid motion is locally induced.

In order to visualize the flow, we observe fluorescent polystyrene particles ($d_{\text{bead}} = 2\ \mu$m, Thermofisher, 488-nm excitation, 508-nm emission) through a Nikon AZ-100 microscope (magnification 3×, numerical aperture equal to 0.1, illumination Nikon Intensilight), capturing particles in focus from all z positions in the cell. Owing to the low numerical aperture of the objective, particles across the entire depth of the channel are imaged simultaneously. We record the particle motion with a scientific complementary metal-oxide semiconductor (sCMOS) camera (ZWO ASI178MM-Cool) at a frame rate of 100 frames/s. Unless otherwise noted, we conduct experiments in an aqueous 4-(2-hydroxyethyl)-1-piperazineethanesulfonic acid (HEPES) buffer solution with an ionic strength of 10 mM at a pH of 7 (see Appendix C for detailed composition). In order to ensure a homogeneous particle distribution over the entire channel height, we match the solution's mass density to that of the particle material by utilizing a 50 vol % D_2O/H_2O solution. All experiments were performed at a temperature of 15 °C.

C. Flow velocity measurements

Before each experiment, we fill the channel with deionized water (Milli-Q) and verify the existence of a stable Cassie-Baxter wetting state by optical inspection. As described by Manukyan *et al.* [44], the Cassie-Baxter and the Wenzel wetting states have different reflectivities under epi-illumination, allowing one to distinguish the wetting states by simple imaging. Afterward, the channel is flushed with the appropriate buffer solution as described. We perform each experiment at a fixed gate voltage over a duration of 60 s, and a series of experiments starts with the lowest gate voltage of 250 V. Successively, we increase the voltage in steps of 250 V, with breaks of approximately 20 s in between the measurements. Since the wetting transition from the Cassie-Baxter to the Wenzel state is irreversible, the experimental data are only usable before such a transition occurs. Also, the transition does not occur over the entire surface at once, but rather appears at one or more separate locations, likely due to local inhomogeneities in the pillar spacing or PVC coating. For the flow field, this leads to a local reduction of the effective slip length, which is easily detectable in the experiments by curved streamlines.

For the processing of the particle tracking velocimetry data, we utilize the MATLAB toolbox PTVLAB [45]. We import the recorded image stacks and in order to prevent any influence of background illumination or of particles adhering to the surface, we create the background image of the observed region by calculating the median image of an image stack. This ensures that local changes in intensity, as occurring due to passing particles, do not propagate into the background image. We subtract this median image from each image in the stack, effectively removing the steady-state background. We compute the velocities of the particles and save them with the corresponding particle positions. Usually, for one fixed gate voltage, we acquire several tens of thousands of particle velocities in the central region of the gate electrode.

Since the average flow field above the electrode is independent of position, all information is preserved by ensemble averaging the N measured particle velocities $\vec{u}_{\text{ROI},i}$ from the central dipole region [region of interest (ROI), as indicated in Fig. 2(c)] as

$$u_{\text{avg}} = \frac{1}{N}\sum_{i=1}^{N} \|\vec{u}_{\text{ROI},i}\|. \tag{6}$$

Figure 2(d) presents the averaged velocity u_{avg} for different pillar spacings at a pH of 7 and a driving field of 50 V/cm. The recorded velocity in the region of interest exhibits a linear dependence on the applied gate voltage in the range from −750 to 750 V and is antisymmetric when reversing the sign of the driving voltage. Due to the increased slip length, higher pillar spacings lead to increased velocities. However, the velocity cannot be indefinitely increased using the gate potential; when the gate voltage exceeds a threshold value, the linear scaling breaks down and we observe a reduction

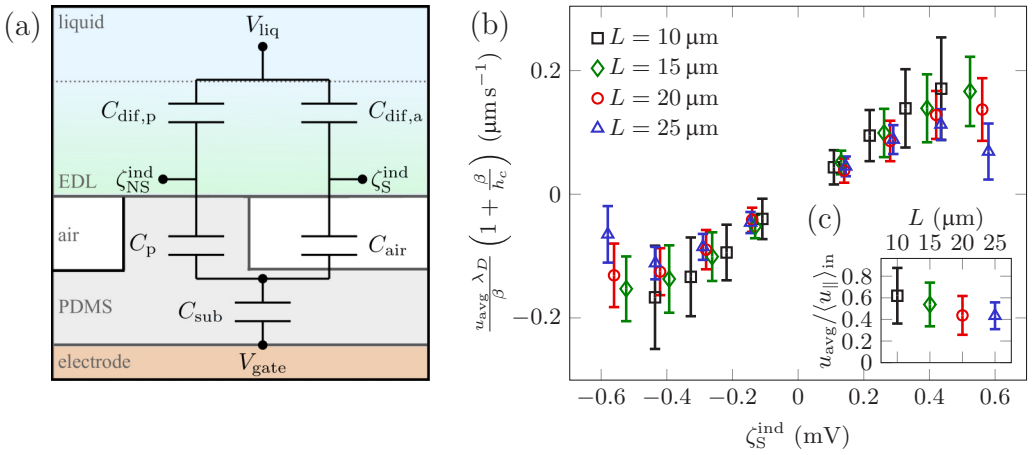

FIG. 3. Scaling of the EOF velocity with theoretical predictions. (a) Electric circuit model used to calculate the induced ζ potential ζ_S^{ind}, which is associated with the induced EOF (see the Supplemental Material [49] for details). (b) Experimental results showing the normalized velocity versus the computed induced potential ζ_S^{ind} according to Eq. (5), where β is calculated based on [47]. The data collapses to one data set, indicating the validity of the theoretical model. (c) Ratio of experimentally measured and theoretically predicted velocity for different pillar periodicities L. The theoretically predicted velocities and the measured velocities show a divergence of about 50%. The error bars represent 95%-confidence intervals based on at least six independent measurements.

in velocity. We attribute this to the wetting transition from the Cassie-Baxter to the Wenzel state induced by Maxwell stresses [44,46].

D. Rescaled flow velocity

In order to validate the theoretical model, we seek to rescale the flow velocity according to Eq. (5), thus requiring models for β and ζ_S^{ind}. Following Davis and Lauga [47] and assuming flat gas-liquid interfaces, disregarding viscous stresses of the enclosed gas or inhomogeneities potentially introduced by the statistical PVC coating, the isotropic slip length can be approximated by

$$\beta = \left(\frac{3}{16}\sqrt{\frac{\pi}{\phi_{PVC}}} - \frac{3}{2\pi}\ln(1+\sqrt{2})\right)L, \tag{7}$$

where ϕ_{PVC} represents the area fraction of the solid-liquid interface.

Following an approach similar to that used by van der Wouden *et al.* in the context of AC field-effect flow control [36,48], we model the induced ζ potentials using an equivalent electric circuit as shown in Fig. 3(a) (a detailed discussion is given in the Supplemental Material [49]). The PDMS layer below the pillars and the air gaps is represented by a capacitance C_{sub}. This layer is in series with two parallel domains representing (i) the pillars and their EDL and (ii) the air gaps and their EDL. We note that this model disregards electric-field lines crossing the pillar sidewalls, as well as any spatial inhomogeneity over the interfaces. We model the capacitances of the PDMS sublayer, pillars, and air gaps as $C_i = \epsilon_i A_i/h_i$, where A_i is the area of the capacitor, h_i the distance between its plates, and ϵ_i its electric permittivity. We approximate the diffuse-layer capacitance using the Gouy-Chapman framework with the differential capacitance $C_{dif,i} = (\epsilon_0\epsilon_{rel,i}/\lambda_D)\cosh(e\zeta/2k_BT)$ [57]. In this model, we also disregard all effects due to surface chemistry and the Stern layer. In general, for solid surfaces these effects can become predominant and suppress the induced charge almost completely [4,5,36]. However, gas-liquid interfaces do not exhibit solid surface chemistry and we do not expect Stern layer adsorption at these interfaces.

Figure 3(b) presents the experimental velocity data rescaled according to Eq. (5) as a function of the computed induced ζ_S^{ind} and shows that the data obtained for different pillar spacings collapse to a single curve. This indicates that the theoretical model captures the scaling behavior of the flow with the solid-liquid area fraction. Interestingly, it also shows that relatively high velocities are induced by very low potentials at the gas-liquid interface, below 1 mV.

Figure 3(c) presents the ratio of the measured velocity u_{avg} and the theoretical dipole velocity $\langle u_{\parallel}\rangle_{in}$, showing that the measured velocities are approximately half of the theoretically predicted ones for all pillar spacings. In the Supplemental Material we have included error estimates for the geometric modeling and the native surface potential, showing that additional effects need to be at play to explain the magnitude of the deviation. Possible explanations include surface conductivity effects or the accumulation of surfactants at the gas-liquid interface. The latter has been reported in similar experiments to cause a significant reduction of the slip length [42,58,59].

E. Comparison to no-slip surfaces

We seek to quantitatively compare the electro-osmotic mobility observed on the SHS with values reported for standard no-slip surfaces. From Eq. (2) we define the wall mobility at a reference viscosity η_{ref} as $\mu_{SHS} = u_{z=0\,\mu m}/E_0 = \epsilon\eta_{ref}^{-1}(\zeta_{NS}^{ind} + \zeta_S^{ind}\beta/\lambda_D)$. From Eq. (5), the depth-averaged velocity at the center of the disk is given by $\langle u_{in}\rangle = \epsilon[4\eta_{expt}(1+\beta/h_c)]^{-1}(\zeta_{NS}^{ind} + \zeta_S^{ind}\beta/\lambda_D)E_0$, where η_{expt} is the viscosity of the electrolyte in the experiment. By substituting one into the other, we obtain an expression for the wall mobility as a function of the measured velocity

$$\mu_{SHS} = 4\langle u_{in}\rangle\left(1+\frac{\beta}{h_c}\right)\eta_r\frac{1}{E_0}, \tag{8}$$

where $\eta_r = \eta_{expt}/\eta_{ref}$ is the ratio of the experimental viscosity and the reference viscosity. Setting the reference as water at room temperature (20 °C), and since our experiments are conducted in 50% D_2O at 15 °C, we obtain $\eta_r = 1.288$ [60,61]. For the largest pillar spacing $L = 25\ \mu$m, the maximum wall mobility (before the transition to the Wenzel state is observed) is $\mu_{SHS} = 1.013 \times 10^{-6}\ m^2/(V\,s)$. Native wall mobilities on glass and polymer surfaces were reported in the range $(2–8) \times 10^{-8}\ m^2/(V\,s)$ [4,5] and wall mobilities induced by gate potentials were reported in the range $(2–6) \times 10^{-8}\ m^2/(V\,s)$ [32,36,41,62]. Hence, the EOF mobilities obtained on our SHSs are at least one order of magnitude larger than those obtained for flat surfaces, both due to charge induction and native surface charge.

F. Influence of the electrolyte

Figure 4(a) presents the flow velocity as a function of the solution *p*H (see Table II in Appendix B for electrolyte compositions), showing no dependence on *p*H for any of the examined surfaces. This is in contrast to native no-slip surfaces, where a *p*H close to the isoelectric point of the surface eliminates the surface charge and thus the EOF velocity. It is also in contrast to the charge induction by gate electrodes, where at specific *p*H values the flow is suppressed completely [4,5,36].

Figure 4(b) presents the flow velocity as a function of the ionic strength for a fixed *p*H. The ionic strength is adjusted from $I = 1$ to 40 mM by adding KCl to a 1 mM HEPES solution. Over the considered interval, the flow velocity decreases by a factor of ~2, even though the electric circuit model presented in Fig. 3(a) predicts no dependence (since increasing the ionic strength lowers both the double-layer thickness λ_D and the surface potential ζ_S^{ind} due to the change in double-layer capacitance C_{dif}). One hypothesis for the observed dependence is surfactant adsorption at the gas-liquid interface, which even at trace amounts can reduce the effective slip length substantially. Since the adsorption of some surfactants increases with salt concentration [63], an increase in concentration could cause a reduction of the effective slip length. However, lacking a rigorous proof, this point remains to be explored in future work.

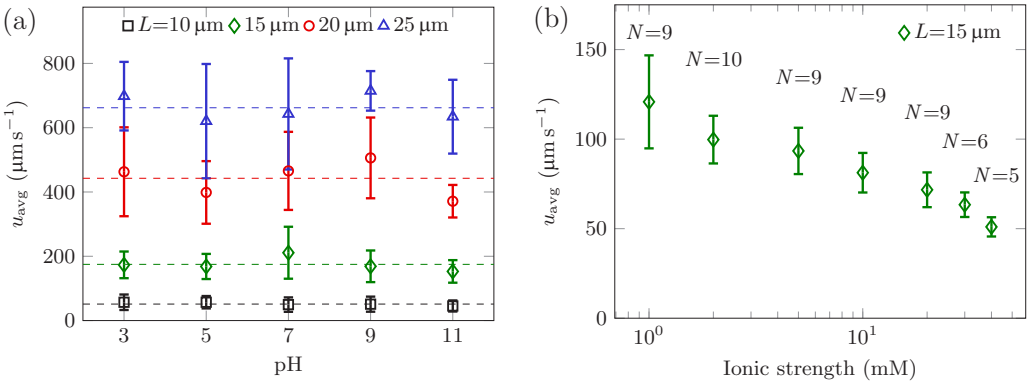

FIG. 4. Experimental results showing the dependence of the depth-averaged EOF velocity on the electrolyte properties. (a) Velocity as a function of *p*H for different pillar periodicity at a constant ionic strength of 10 mM and $V_{\text{gate}} = 500$ V. The dashed lines represent the averages over all *p*H values for the different surfaces. Error bars represent the 90%-confidence interval based on five independent measurements. (b) Velocity as a function of ionic strength for a pillar periodicity of $L = 15$ μm at $V_{\text{gate}} = 250$ V and a fixed *p*H of 7. Here N represents the number of independent measurements taken.

III. CONCLUSION

In this work, we have demonstrated the enhancement of electro-osmotic flow over superhydrophobic surfaces using gate electrodes. The charges created at the gas-liquid interface couple to the external electric field, giving rise to maximum flow velocities that exceed the velocities observed on flat solid surfaces by at least an order of magnitude. The demonstrated scaling with $\zeta_S^{\text{ind}}\beta/\lambda_D$ suggests future strategies to further enhance the induced velocities. For example, utilizing superoleophobic surfaces as reported in the literature [64–67], which are even more stable against wetting transitions, could enable higher induced potentials and thus higher velocities. Traditional EOF pumps offer low flow rates, yet enable very high pressures [68,69]. Electro-osmotic flow over a SHS provides a different work point for EOF pumps, where much higher flow rates can be achieved, but pressures are limited by the stability of the wetting state. Also, in contrast to the irreversible dielectric breakdown of gate electrode materials used for flat surfaces, drying and refilling a collapsed SHS cell renders it useful again.

Additionally, our work could provide opportunities for investigation in various research fields. For example, Fan *et al.* [70] recently showed that pressure-driven flow over superhydrophobic surfaces with oil-filled indentations yields higher streaming potentials than air-filled indentations. The higher streaming potential could be explained by higher potential at the slipping surface for oil. By inducing charge at the interface, a similar enhancement of streaming potential for air-filled indentations could be leveraged for power conversion applications. Another particularly interesting property is the independence of the flow on the solution *p*H, which could be utilized for laboratory-on-a-chip applications where the *p*H of samples can vary drastically. In combination with the ability to dynamically control the flow patterns using multiple electrodes, we believe that EOF over superhydrophobic surfaces could be used in biochemical and high-throughput applications that were not accessible before.

ACKNOWLEDGMENTS

The authors thank K. Gommed for continuous help with the microfabrication. We also thank the Micro-Nano-Fabrication & Printing Unit at Technion for access to the cleanroom facilities. This research was supported by the German-Israeli Foundation for Scientific Research and Development through Grant No. I-1346-401.10/2016.

APPENDIX A: GOVERNING EQUATIONS

We here derive the governing equations for the fluid flow in analogy to Ref. [42], with additionally accounting for slip at the lower wall. The model system consists of a shallow flow cell with arbitrary surface potentials ζ_{U}, ζ_{S}, and ζ_{NS}, corresponding to the upper wall, the lower wall at slip regions, and the lower wall at no-slip regions, respectively. The characteristic length in the vertical direction is defined by the cell height h_c and the lateral characteristic length scale is defined by the typical length L over which the ζ potentials vary.

We assume a shallow flow regime ($\epsilon = h_c/L \ll 1$) and negligible inertia ($\epsilon\,\mathrm{Re} = \epsilon\rho U h_c/\eta \ll 1$). The typical velocity in the axial direction U is given by the Helmholtz-Smoluchowski expression for the EOF velocity as $U = -\epsilon\zeta_{\mathrm{ref}}E_{\mathrm{ref}}/\eta$, where ϵ is the electric permittivity, ζ_{ref} is a typical ζ potential, E_{ref} is a characteristic electric field in the fluidic cell, and η is the fluid's dynamic viscosity. The characteristic potential ζ_{ref} can be defined as the characteristic surface potential at the gas-liquid interface due to the charge induction of the gate electrode. The characteristic electric-field strength follows from the applied electric field inside the cell that is assumed to be uniform over the fluidic domain of interest. This is valid for small Dukhin numbers ($\mathrm{Du} = \sigma_s/\sigma_b L \ll \epsilon$) [71], where σ_s and σ_b are the surface and bulk conductivity, respectively. A characteristic timescale follows from the characteristic length scale and velocity as $T = L/U$. The characteristic scales for the pressure p_{ref} and the velocity W in the z direction, however, are unknown *a priori* and follow from scaling arguments.

Introducing the nondimensional variables (denoted by tildes) $(\tilde{x}, \tilde{y}, \tilde{z}) = (x/L, y/L, z/h_c)$, $\tilde{t} = t/T$, $(\tilde{u}, \tilde{v}, \tilde{w}) = (u/U, v/U, w/W)$, $\tilde{p} = p/p_{\mathrm{ref}}$, $\tilde{\zeta} = \zeta/\zeta_{\mathrm{ref}}$, and $\vec{\tilde{E}} = \vec{E}/E_{\mathrm{ref}}$ in combination with an order-of-magnitude analysis of the continuity and the Navier-Stokes equations leads to expressions for the characteristic vertical velocity $W = \epsilon U$ and the pressure scale $p_{\mathrm{ref}} = -\epsilon_0\zeta_{\mathrm{ref}}E_{\mathrm{ref}}/\epsilon^2 L$. A leading-order expansion in ϵ of the continuity and the Navier Stokes equations yields

$$0 = \frac{\partial\tilde{u}}{\partial\tilde{x}} + \frac{\partial\tilde{v}}{\partial\tilde{y}} + \frac{\partial\tilde{w}}{\partial\tilde{z}}, \tag{A1a}$$

$$\vec{\tilde{\nabla}}_{\parallel}\tilde{p} = \frac{\partial^2\vec{\tilde{u}}_{\parallel}}{\partial\tilde{z}^2} + O(\epsilon\,\mathrm{Re}, \epsilon^2), \tag{A1b}$$

$$\frac{\partial\tilde{p}}{\partial\tilde{z}} = O(\epsilon^3\mathrm{Re}, \epsilon^2). \tag{A1c}$$

In what follows, we deviate from the reported derivation by incorporating the effect of the superhydrophobic surface at the lower wall by an effective wall boundary condition in accordance with Schönecker and Hardt [38]. Here the effective slip length is assumed to be uniform and isotropic over the whole surface. For brevity, we assume that the gas-liquid interfaces are perfectly slipping, so that the viscosity of the enclosed gas has no influence on the flow. The boundary condition then reads

$$\vec{u}_{\parallel}|_{z=0\,\mu\mathrm{m}} = -\frac{\epsilon\vec{E}_{\parallel}}{\eta}\left(\zeta_{\mathrm{NS}} + \zeta_{\mathrm{S}}\frac{\beta}{\lambda_D}\right) + \beta\left.\frac{\partial\vec{u}_{\parallel}}{\partial z}\right|_{z=0\,\mu\mathrm{m}}. \tag{A2}$$

For typical pillar spacings of the order of 10 μm, the ratio β/λ_D can be of the order of 10^3–10^4, outlining the flow enhancement potential even for small ζ_{S}.

Integrating Eq. (A1b) twice in the z direction and accounting for the boundary condition (A2) at the lower wall and the no-slip condition at the top wall leads to an expression for the nondimensional velocity:

$$\begin{aligned}\vec{\tilde{u}}_{\parallel} = {} & \frac{1}{2}\vec{\tilde{\nabla}}_{\parallel}\tilde{p}\tilde{z}^2 + \frac{1}{1+\frac{\beta}{h_c}}\left\{\tilde{z}\left[\vec{\tilde{E}}_{\parallel}\left(\tilde{\zeta}_{\mathrm{U}} - \tilde{\zeta}_{\mathrm{NS}} - \frac{\beta}{\lambda_D}\tilde{\zeta}_{\mathrm{S}}\right) - \frac{1}{2}\vec{\tilde{\nabla}}_{\parallel}\tilde{p}\right]\right. \\ & \left. + \left[\vec{\tilde{E}}_{\parallel}\left(\frac{\beta}{h_c}\tilde{\zeta}_{\mathrm{U}} + \tilde{\zeta}_{\mathrm{NS}} + \frac{\beta}{\lambda_D}\tilde{\zeta}_{\mathrm{S}}\right) - \frac{1}{2}\frac{\beta}{h_c}\vec{\tilde{\nabla}}_{\parallel}\tilde{p}\right]\right\}.\end{aligned} \tag{A3}$$

By integrating over the channel height, the depth-averaged velocity is obtained as

$$\langle \vec{\tilde{u}}_\parallel \rangle = -\frac{1+4\frac{\beta}{h_c}}{12\left(1+\frac{\beta}{h_c}\right)}\vec{\tilde{\nabla}}_\parallel \tilde{p} + \frac{1}{2\left(1+\frac{\beta}{h_c}\right)}\vec{\tilde{E}}_\parallel\left[\left(1+2\frac{\beta}{h_c}\right)\tilde{\zeta}_\mathrm{U} + \tilde{\zeta}_\mathrm{NS} + \frac{\beta}{\lambda_D}\tilde{\zeta}_\mathrm{S}\right]. \tag{A4}$$

We note that by setting the slip length to zero, the second term on the right-hand side of Eq. (A4) would reduce to an average surface potential that can be calculated by the arithmetic average of the two potentials as $\langle \tilde{\zeta} \rangle = \frac{1}{2}(\tilde{\zeta}_\mathrm{U} + \tilde{\zeta}_\mathrm{NS})$, corresponding to the original expression for the velocity [42].

In analogy to Ref. [42], a set of two independent Poisson equations for the pressure p and the stream function $\tilde{\psi}$ is obtained by applying the two-dimensional divergence $\vec{\tilde{\nabla}}_\parallel \cdot$ and the two-dimensional curl $\vec{\tilde{\nabla}}_\parallel \times$ operators to Eq. (A4), respectively,

$$\tilde{\nabla}_\parallel^2 \tilde{p} = \frac{6}{1+\frac{\beta}{h_c}}\vec{\tilde{E}}_\parallel \cdot \left[\left(1+2\frac{\beta}{h_c}\right)\vec{\tilde{\nabla}}_\parallel \tilde{\zeta}_\mathrm{U} + \vec{\tilde{\nabla}}_\parallel \tilde{\zeta}_\mathrm{NS} + \frac{\beta}{\lambda_D}\vec{\tilde{\nabla}}_\parallel \tilde{\zeta}_\mathrm{S}\right], \tag{A5}$$

$$\tilde{\nabla}_\parallel^2 \tilde{\psi} = \frac{1}{2\left(1+\frac{\beta}{h_c}\right)}\vec{\tilde{E}}_\parallel \times \left[\left(1+2\frac{\beta}{h_c}\right)\vec{\tilde{\nabla}}_\parallel \tilde{\zeta}_\mathrm{U} + \vec{\tilde{\nabla}}_\parallel \tilde{\zeta}_\mathrm{NS} + \frac{\beta}{\lambda_D}\vec{\tilde{\nabla}}_\parallel \tilde{\zeta}_\mathrm{S}\right]\vec{e}_z, \tag{A6}$$

where the stream function $\tilde{\psi}$ is defined via $\langle \vec{\tilde{u}}_\parallel \rangle = (\partial\tilde{\psi}/\partial\tilde{y}, -\partial\tilde{\psi}/\partial\tilde{x})$. These governing equations enable us to determine the flow field for a given ζ potential distribution. Due to the presence of the superhydrophobic surface, the equations include a more complex averaging of the ζ potentials than the arithmetic average of [42]. The original form of the governing equations can be recovered by introducing the following generalized averaging of the ζ potential distribution:

$$\langle \tilde{\zeta} \rangle_\mathrm{SHS} = \frac{1}{2\left(1+4\frac{\beta}{h_c}\right)}\left[\left(1+2\frac{\beta}{h_c}\right)\tilde{\zeta}_\mathrm{U} + \tilde{\zeta}_\mathrm{NS} + \frac{\beta}{\lambda_D}\tilde{\zeta}_\mathrm{S}\right]. \tag{A7}$$

By introducing a transformed stream function ψ_SHS as

$$\tilde{\psi}_\mathrm{SHS} = \frac{1+\frac{\beta}{h_c}}{1+4\frac{\beta}{h_c}}\tilde{\psi}, \tag{A8}$$

the set of governing equations is rewritten as

$$\tilde{\nabla}_\parallel^2 \tilde{p} = 12\vec{\tilde{E}}_\parallel \cdot \vec{\tilde{\nabla}}_\parallel \langle \tilde{\zeta} \rangle_\mathrm{SHS}, \tag{A9a}$$

$$\tilde{\nabla}_\parallel^2 \tilde{\psi}_\mathrm{SHS} = (\vec{\tilde{E}}_\parallel \times \vec{\tilde{\nabla}}_\parallel \langle \tilde{\zeta} \rangle_\mathrm{SHS}) \cdot \vec{e}_z, \tag{A9b}$$

with

$$\langle \vec{\tilde{u}}_\parallel \rangle = \frac{1+4\frac{\beta}{h_c}}{1+\frac{\beta}{h_c}}(\partial\tilde{\psi}_\mathrm{SHS}/\partial\tilde{y}, -\partial\psi_\mathrm{SHS}/\partial\tilde{x}). \tag{A10}$$

Since this transformation recovers the original governing equations [39], from here on the mathematical treatment is analogous to that of Boyko and co-workers. In that context, we are especially interested in the flow field for a ζ_SHS potential induced in a disk-shaped region. In the following, for convenience, we summarize the results, but for details, the interested reader is referred to the original work [42].

The corresponding ζ_SHS potential distribution reads

$$\langle \tilde{\zeta} \rangle_\mathrm{SHS} = \langle \tilde{\zeta} \rangle_0 H(\tilde{r}_0 - \tilde{r}), \tag{A11}$$

where $\tilde{r}_0$ is the radius of the circular region, $\tilde{r}$ the radial coordinate, H the Heaviside step function, and $\langle\zeta\rangle_0$ the value of $\langle\zeta\rangle_{\mathrm{SHS}}$ above the electrode. For such a distribution and an electric field in the x direction [$\vec{\tilde{E}}_\parallel = (\tilde{E}_0, 0)$], the pressure field takes the following form in polar coordinates:

$$p(r,\Theta) = \begin{cases} \left(\frac{a_{\mathrm{out}}}{r} + b_{\mathrm{out}}\tilde{r}\right)\cos\Theta, & \tilde{r} > \tilde{r}_0 \quad \text{(A12a)} \\ b_{\mathrm{in}}\tilde{r}\cos\Theta, & \tilde{r} < \tilde{r}_0. \quad \text{(A12b)} \end{cases}$$

Inserting this pressure distribution into Eq. (A4) leads to an expression for the velocity distribution

$$\langle\vec{\tilde{u}}_\parallel\rangle(\tilde{r},\Theta) = \begin{cases} \frac{1+4\frac{\beta}{h_c}}{1+\frac{\beta}{h_c}}\left[\frac{1}{12}\left(-b_{\mathrm{out}}+\frac{a_{\mathrm{out}}}{\tilde{r}^2}\right)\cos\Theta\vec{e}_r+\frac{1}{12}\left(b_{\mathrm{out}}+\frac{a_{\mathrm{out}}}{\tilde{r}^2}\right)\sin\Theta\vec{e}_\Theta\right], & \tilde{r} > \tilde{r}_0 \quad \text{(A13a)} \\ \frac{1+4\frac{\beta}{h_c}}{1+\frac{\beta}{h_c}}\left[\left(-\frac{1}{12}b_{\mathrm{in}}+\tilde{E}_0\langle\tilde{\zeta}\rangle_0\right)\cos\Theta\vec{e}_r+\left(\frac{1}{12}b_{\mathrm{in}}-\tilde{E}_0\langle\tilde{\zeta}\rangle_0\right)\sin\Theta\vec{e}_\Theta\right], & \tilde{r} < \tilde{r}_0, \quad \text{(A13b)} \end{cases}$$

where $\vec{e}_r$ and $\vec{e}_\Theta$ are the unit vectors in polar coordinates. Above the circular electrode, the velocity is uniform due to the constant pressure gradient, leading to

$$\langle\vec{\tilde{u}}_\parallel\rangle_{\mathrm{in}} = \frac{1+4\frac{\beta}{h_c}}{1+\frac{\beta}{h_c}}\left(-\frac{1}{12}b_{\mathrm{in}} + E_0\langle\tilde{\zeta}\rangle_0\right)\vec{e}_x. \quad \text{(A14)}$$

The circular $\langle\tilde{\zeta}\rangle_{\mathrm{SHS}}$ potential distribution creates a dipole flow field. Because of the uniformity of the flow above the electrode, such a flow field is ideal to evaluate the effect of induced ζ potentials.

By requiring continuity of the pressure as well as the radial velocity at $\tilde{r} = \tilde{r}_0$ and prescribing a constant pressure far away from the electrode, the coefficients in Eqs. (A13a) and (A13b) can be determined as

$$a_{\mathrm{out}} = 6\tilde{E}_0\langle\tilde{\zeta}\rangle_0\tilde{r}_0^2, \quad \text{(A15)}$$

$$b_{\mathrm{in}} = 6\tilde{E}_0\langle\tilde{\zeta}\rangle_0, \quad \text{(A16)}$$

$$b_{\mathrm{out}} = 0. \quad \text{(A17)}$$

They can be interpreted physically as follows: a_{out} is the dipole strength, b_{in} is the pressure gradient in the direction of the electric field inside the circular region, and b_{out} is the externally applied pressure gradient. As a final result, the velocity in the inner region follows as

$$\langle\vec{\tilde{u}}_\parallel\rangle_{\mathrm{in}} = \frac{1+4\frac{\beta}{h_c}}{1+\frac{\beta}{h_c}}\left(\frac{1}{2}E_0\langle\tilde{\zeta}\rangle_0\right)\vec{e}_x. \quad \text{(A18)}$$

This result is valid for the theoretically predicted velocity in the central region of the dipole flow. Rewriting in dimensional variables yields Eq. (5).

APPENDIX B: PRODUCTION OF SUPERHYDROPHOBIC SURFACES AND MICROFLUIDIC DEVICE

The microstructured surface is produced by a standard soft-lithography replica method. First, a master structure on a silicon wafer is produced by deep reactive ion etching and is silanized by evaporation of trimethylsilane in a closed vacuum bell. We repeat the silanization process prior to every molding process, to prevent sticking of the elastomer.

The positive replica is produced from polydimethylsiloxane (Dow Sylgard 184 silicone elastomer) with an elastomer–cross-linker ratio of 10:1. First, we mix the components thoroughly and afterward degas them in vacuum to minimize air entrapment. Successively, the elastomer is spin coated on the silicon master, first for 40 s at 200 rpm, followed by 40 s at 600 rpm. Afterward, we

TABLE II. Buffer composition for the *p*H dependence measurements. All experiments were done with a fixed ionic strength of $I = 10$ mM. The *p*H value is adjusted by using a weak base or acid and shifting the chemical equilibrium with a strong acid or base as titrant, respectively. The ionic strengths as well as buffer capacitances of the solutions are calculated with PEAKMASTER 5.3 [72].

*p*H value	Buffer (weak electrolyte)[a]	Concentration c_{buf} (mM)	Titrant (strong acid or base)	Concentration c_{tit} (mM)
3	citric acid	20	NaOH	9
5	creatinine	20	HCl	10
7	HEPES	42.85	NaOH	10
9	histidine	26	NaOH	10
11	histidine	9	NaOH	10

[a]Acquired from Sigma-Aldrich.

place the wafer inside an oven for 3 h at 85 °C. In the next step, we peel the elastic sheet off the mask with special care not to damage the microstructured layer. Since one mask accommodates up to ten surfaces, we cut the sheet and place the pieces on glass slides, with the pillars pointing upward. We show the geometric parameters in Fig. 1(b).

Next we pattern the microstructures with a secondary nanostructure made of PVC, based on the work of Chen and co-workers [39]. Briefly, we dissolve 50 mg of polyvinyl chloride (Sigma-Aldrich, high molecular weight, product No. 81387) in 10 ml of tetrahydrofurane (THF) and then add 10 ml of ethanol to the solution. Ethanol is a nonsolvent for PVC and during evaporation, PVC starts to precipitate out of the solution and forms crystals. The crystal structure and particle size can be influenced by the ratio of ethanol to THF, with higher ethanol fractions leading to smaller particles. During evaporation of the applied solution to the surfaces, PVC particles attach to the pillars of the microstructured surface.

The final microstructured surfaces have pillar spacings as described in Table I. The surfaces with a pitch of $L = 10$ μm have a pillar height of 10 μm and a sublayer thickness of 130 μm, whereas the other surface types have a pillar height of 15 μm and a sublayer height of 120 μm. All pillars have a square shape with rounded edges. Due to the added PVC, the pillars become wider and the shape becomes more irregular. By evaluation of scanning electron microscopy (SEM) images of the surfaces, we estimate that the pillar can be approximated as a circle with a diameter of 6.5 μm. Table I also contains the predicted slip length according to Davis and Lauga based on the effective diameter of the pillars [47].

In order to produce the microfluidic device, we produce several gate electrodes on top of a glass wafer using vapor deposition (Balzers BAK 600) of chrome and a standard lift-off process using a positive photoresist (AZ 9260). Afterward, the wafer is diced to have only one electrode per piece. We activate the wafer containing the electrodes as well as the back side of the microstructured PDMS by oxygen plasma (Diener Femto plasma cleaner, 20 s, 50 W) and put them in contact to form a permanent bond. This structure serves as the floor of the cell. As a ceiling, we use glass slides cut to size, with holes drilled for liquid access. We seal the cell by applying UV-cured optical glue (Thorlabs, NOA68) to the lateral restrictions of the bottom structure. On top of the holes of the glass slide we place punched pieces of PDMS serving as reservoirs.

APPENDIX C: LIQUID COMPOSITIONS

Unless otherwise noted, we used the buffer solutions listed in Table II, providing a range of *p*H values at a fixed ionic strength of 10 mM. As also mentioned in Sec. II B, we performed all experiments in a mixture of 50 : 50 vol % D_2O/H_2O. For the experiments with varying ionic strength, we used a HEPES-NaOH buffer at an ionic strength of 1 mM and added KCl to reach the desired ionic strength.

[1] M. von Smoluchowski, in *Handbuch der Elektrizität und des Magnetismus*, edited by L. Graetz (Barth, Leipzig, 1921), Vol. 2.
[2] D. Burgreen and F. R. Nakache, Electrokinetic flow in ultrafine capillary slits 1, J. Phys. Chem. **68**, 1084 (1964).
[3] C. L. Rice and R. Whitehead, Electrokinetic flow in a narrow cylindrical capillary, J. Phys. Chem. **69**, 4017 (1965).
[4] B. J. Kirby and E. F. Hasselbrink, Zeta potential of microfluidic substrates: 1. Theory, experimental techniques, and effects on separations, Electrophoresis **25**, 187 (2004).
[5] B. J. Kirby and E. F. Hasselbrink, Zeta potential of microfluidic substrates: 2. Data for polymers, Electrophoresis **25**, 203 (2004).
[6] J. R. Melcher and G. I. Taylor, Electrohydrodynamics: A Review of the role of interfacial shear stresses, Annu. Rev. Fluid Mech. **1**, 111 (1969).
[7] O. I. Vinogradova, Slippage of water over hydrophobic surfaces, Int. J. Miner. Process. **56**, 31 (1999).
[8] R. Pit, H. Hervet, and L. Léger, Friction and slip of a simple liquid at a solid surface, Tribol. Lett. **7**, 147 (1999).
[9] S. Jin, P. Huang, J. Park, J. Y. Yoo, and K. S. Breuer, Near-surface velocimetry using evanescent wave illumination, Exp. Fluids **37**, 825 (2004).
[10] P. Joseph and P. Tabeling, Direct measurement of the apparent slip length, Phys. Rev. E **71**, 035303(R) (2005).
[11] E. Lauga, M. P. Brenner, and H. A. Stone, in *Handbook of Experimental Fluid Dynamics*, edited by C. Tropea, A. L. Yarin, and J. F. Foss (Springer, Berlin, 2007), Chap. 19, pp. 1219–1240.
[12] M.-C. Audry, A. Piednoir, P. Joseph, and E. Charlaix, Amplification of electro-osmotic flows by wall slippage: Direct measurements on OTS-surfaces, Faraday Discuss. **146**, 113 (2010).
[13] L. Joly, C. Ybert, E. Trizac, and L. Bocquet, Hydrodynamics within the Electric Double Layer on Slipping Surfaces, Phys. Rev. Lett. **93**, 257805 (2004).
[14] N. Churaev, J. Ralston, I. Sergeeva, and V. Sobolev, Electrokinetic properties of methylated quartz capillaries, Adv. Colloid Interface Sci. **96**, 265 (2002).
[15] H. Stone, A. Stroock, and A. Ajdari, Engineering flows in small devices, Annu. Rev. Fluid Mech. **36**, 381 (2004).
[16] A. Ajdari and L. Bocquet, Giant Amplification of Interfacially Driven Transport by Hydrodynamic Slip: Diffusio-Osmosis and Beyond, Phys. Rev. Lett. **96**, 186102 (2006).
[17] C. I. Bouzigues, P. Tabeling, and L. Bocquet, Nanofluidics in the Debye Layer at Hydrophilic and Hydrophobic Surfaces, Phys. Rev. Lett. **101**, 114503 (2008).
[18] T. M. Squires, Electrokinetic flows over inhomogeneously slipping surfaces, Phys. Fluids **20**, 092105 (2008).
[19] J. Ou, B. Perot, and J. P. Rothstein, Laminar drag reduction in microchannels using ultrahydrophobic surfaces, Phys. Fluids **16**, 4635 (2004).
[20] C.-H. Choi and C.-J. Kim, Large Slip of Aqueous Liquid Flow over a Nanoengineered Superhydrophobic Surface, Phys. Rev. Lett. **96**, 066001 (2006).
[21] P. Joseph, C. Cottin-Bizonne, J.-M. Benoît, C. Ybert, C. Journet, P. Tabeling, and L. Bocquet, Slippage of Water Past Superhydrophobic Carbon Nanotube Forests in Microchannels, Phys. Rev. Lett. **97**, 156104 (2006).
[22] C. Ybert, C. Barentin, C. Cottin-Bizonne, P. Joseph, and L. Bocquet, Achieving large slip with superhydrophobic surfaces: Scaling laws for generic geometries, Phys. Fluids **19**, 123601 (2007).
[23] C. Lee, C.-H. Choi, and C.-J. Kim, Structured Surfaces for a Giant Liquid Slip, Phys. Rev. Lett. **101**, 064501 (2008).
[24] J. P. Rothstein, Slip on superhydrophobic surfaces, Annu. Rev. Fluid Mech. **42**, 89 (2010).
[25] S. S. Bahga, O. I. Vinogradova, and M. Z. Bazant, Anisotropic electro-osmotic flow over superhydrophobic surfaces, J. Fluid Mech. **644**, 245 (2010).
[26] A. V. Belyaev and O. I. Vinogradova, Electro-osmosis on Anisotropic Superhydrophobic Surfaces, Phys. Rev. Lett. **107**, 098301 (2011).

[27] D. M. Huang, C. Cottin-Bizonne, C. Ybert, and L. Bocquet, Massive Amplification of Surface-Induced Transport at Superhydrophobic Surfaces, Phys. Rev. Lett. **101**, 064503 (2008).
[28] C. S. Lee, W. C. Blanchard, and C. T. Wu, Direct control of the electroosmosis in capillary zone electrophoresis by using an external electric field, Anal. Chem. **62**, 1550 (1990).
[29] N. G. Green, A. Ramos, A. González, H. Morgan, and A. Castellanos, Fluid flow induced by nonuniform ac electric fields in electrolytes on microelectrodes. I. Experimental measurements, Phys. Rev. E **61**, 4011 (2000).
[30] A. González, A. Ramos, N. G. Green, A. Castellanos, and H. Morgan, Fluid flow induced by nonuniform ac electric fields in electrolytes on microelectrodes. II. A linear double-layer analysis, Phys. Rev. E **61**, 4019 (2000).
[31] N. G. Green, A. Ramos, A. González, H. Morgan, and A. Castellanos, Fluid flow induced by nonuniform ac electric fields in electrolytes on microelectrodes. III. Observation of streamlines and numerical simulation, Phys. Rev. E **66**, 026305 (2002).
[32] R. B. M. Schasfoort, S. Schlautmann, J. Hendrikse, and A. van den Berg, Field-effect row control for microfabricated fluidic networks, Science **286**, 942 (1999).
[33] S. Mutlu, F. Svec, C. Mastrangelo, J. Frechet, and Y. Gianchandani, in *Proceedings of the 17th IEEE International Conference on Micro Electro Mechanical Systems, Maastricht, 2004* (IEEE, Piscataway, 2004), pp. 850–853.
[34] N. J. Sniadecki, C. S. Lee, P. Sivanesan, and D. L. DeVoe, Induced pressure pumping in polymer microchannels via field-effect flow control, Anal. Chem. **76**, 1942 (2004).
[35] K. Horiuchi and P. Dutta, Electrokinetic flow control in microfluidic chips using a field-effect transistor, Lab Chip **6**, 714 (2006).
[36] E. J. van der Wouden, D. C. Hermes, J. G. E. Gardeniers, and A. van den Berg, Directional flow induced by synchronized longitudinal and zeta-potential controlling AC-electrical fields, Lab Chip **6**, 1300 (2006).
[37] C. Steffes, T. Baier, and S. Hardt, Enabling the enhancement of electroosmotic flow over superhydrophobic surfaces by induced charges, Colloids Surf. A **376**, 85 (2011).
[38] C. Schönecker and S. Hardt, Electro-osmotic flow along superhydrophobic surfaces with embedded electrodes, Phys. Rev. E **89**, 063005 (2014).
[39] E. Boyko, S. Rubin, A. D. Gat, and M. Bercovici, Flow patterning in Hele-Shaw configurations using non-uniform electro-osmotic slip, Phys. Fluids **27**, 102001 (2015).
[40] F. Paratore, E. Boyko, G. V. Kaigala, and M. Bercovici, Electroosmotic Flow Dipole: Experimental Observation and Flow Field Patterning, Phys. Rev. Lett. **122**, 224502 (2019).
[41] F. Paratore, V. Bacheva, G. V. Kaigala, and M. Bercovici, Dynamic microscale flow patterning using electrical modulation of zeta potential, Proc. Natl. Acad. Sci. USA **116**, 10258 (2019).
[42] D. Schäffel, K. Koynov, D. Vollmer, H.-J. Butt, and C. Schönecker, Local Flow Field and Slip Length of Superhydrophobic Surfaces, Phys. Rev. Lett. **116**, 134501 (2016).
[43] H. Chen, Z. Yuan, J. Zhang, Y. Liu, K. Li, D. Zhao, S. Li, P. Shi, and J. Tang, Preparation, characterization and wettability of porous superhydrophobic poly (vinyl chloride) surface, J. Porous Mater. **16**, 447 (2009).
[44] G. Manukyan, J. M. Oh, D. van den Ende, R. G. H. Lammertink, and F. Mugele, Electrical Switching of Wetting States on Superhydrophobic Surfaces: A Route Towards Reversible Cassie-to-Wenzel Transitions, Phys. Rev. Lett. **106**, 014501 (2011).
[45] W. Brevis, Y. Niño, and G. H. Jirka, Integrating cross-correlation and relaxation algorithms for particle tracking velocimetry, Exp. Fluids **50**, 135 (2011).
[46] J. M. Oh, G. Manukyan, D. V. D. Ende, and F. Mugele, Electric-field–driven instabilities on superhydrophobic surfaces, Europhys. Lett. **93**, 56001 (2011).
[47] A. M. J. Davis and E. Lauga, Hydrodynamic friction of fakir-like superhydrophobic surfaces, J. Fluid Mech. **661**, 402 (2010).
[48] E. van der Wouden, T. Heuser, D. Hermes, R. Oosterbroek, J. Gardeniers, and A. van den Berg, Field-effect control of electro-osmotic flow in microfluidic networks, Colloids Surf. A **267**, 110 (2005).
[49] See Supplemental Material at http://link.aps.org/supplemental/10.1103/PhysRevFluids.5.053701 for information about the electric circuit model and a movie, which includes Refs. [50–56].

[50] R. J. Hunter, in *Zeta Potential in Colloid Science: Principles and Applications*, edited by R. H. Ottewill and R. L. Rowell (Academic, New York, 2013), Vol. 2.
[51] P. J. Roache, Perspective: A method for uniform reporting of grid refinement studies, J. Fluids Eng. **116**, 405 (1994).
[52] P. Leroy, D. Jougnot, A. Revil, A. Lassin, and M. Azaroual, A double layer model of the gas bubble/water interface, J. Colloid Interface Sci. **388**, 243 (2012).
[53] C. Yang, T. Dabros, D. Li, J. Czarnecki, and J. H. Masliyah, Measurement of the zeta potential of gas bubbles in aqueous solutions by microelectrophoresis method, J. Colloid Interface Sci. **243**, 128 (2001).
[54] A. S. Najafi, J. Drelich, A. Yeung, Z. Xu, and J. Masliyah, A novel method of measuring electrophoretic mobility of gas bubbles, J. Colloid Interface Sci. **308**, 344 (2007).
[55] W. Jia, S. Ren, and B. Hu, Effect of water chemistry on zeta potential of air bubbles, Int. J. Electrochem. Sci. **8**, 5828 (2013).
[56] M. Takahashi, ζ potential of microbubbles in aqueous solutions: Electrical properties of the gas-water interface, J. Phys. Chem. B **109**, 21858 (2005).
[57] H. Butt, K. Graf, and M. Kappl, *Physics and Chemistry of Interfaces* (Wiley, New York, 2003), Vol. 50, pp. 135–147.
[58] F. J. Peaudecerf, J. R. Landel, R. E. Goldstein, and P. Luzzatto-Fegiz, Traces of surfactants can severely limit the drag reduction of superhydrophobic surfaces, Proc. Natl. Acad. Sci. USA **114**, 7254 (2017).
[59] L. Joly, F. Detcheverry, and A.-L. Biance, Anomalous ζ Potential in Foam Films, Phys. Rev. Lett. **113**, 088301 (2014).
[60] J. Kestin, N. Imaishi, S. Nott, J. Nieuwoudt, and J. Sengers, Viscosity of light and heavy water and their mixtures, Physica A **134**, 38 (1985).
[61] R. C. Hardy and R. L. Cottington, Viscosity of deuterium oxide and water in the range 5° to 125° C, J. Res. Natl. Bur. Stand. **42**, 573 (1949).
[62] L.-C. Chen, C.-C. Wu, R.-G. Wu, and H.-C. Chang, Electroosmotic flow control in microfluidic chips using a self-assembled monolayer as the insulator of a flow field-effect transistor, Langmuir **28**, 11281 (2012).
[63] K. Tajima, Radiotracer studies on adsorption of surface active substance at aqueous surface. III. The effects of salt on the adsorption of sodium dodecylsulfate, Bull. Chem. Soc. Jpn. **44**, 1767 (1971).
[64] A. Tuteja, W. Choi, M. Ma, J. M. Mabry, S. A. Mazzella, G. C. Rutledge, G. H. McKinley, and R. E. Cohen, Designing superoleophobic surfaces, Science **318**, 1618 (2007).
[65] E. Gogolides, K. Ellinas, and A. Tserepi, Hierarchical micro and nano structured, hydrophilic, superhydrophobic and superoleophobic surfaces incorporated in microfluidics, microarrays and laboratory on chip microsystems, Microelectron. Eng. **132**, 135 (2015).
[66] H. Teisala and H.-J. Butt, Hierarchical structures for superhydrophobic and superoleophobic surfaces, Langmuir **35**, 10689 (2019).
[67] Z. Dong, M. F. Schumann, M. J. Hokkanen, B. Chang, A. Welle, Q. Zhou, R. H. A. Ras, Z. Xu, M. Wegener, and P. A. Levkin, Superoleophobic slippery lubricant-infused surfaces: Combining two extremes in the same surface, Adv. Mater. **30**, 1803890 (2018).
[68] S. Zeng, C.-H. Chen, J. C. Mikkelsen, Jr., and J. G. Santiago, Fabrication and characterization of electroosmotic micropumps, Sens. Actuat. B **79**, 107 (2001).
[69] J. A. Tripp, F. Svec, J. M. Fréchet, S. Zeng, J. C. Mikkelsen, and J. G. Santiago, High-pressure electroosmotic pumps based on porous polymer monoliths, Sens. Actuat. B **99**, 66 (2004).
[70] B. Fan, A. Bhattacharya, and P. R. Bandaru, Enhanced voltage generation through electrolyte flow on liquid-filled surfaces, Nat. Commun. **9**, 4050 (2018).
[71] A. S. Khair and T. M. Squires, Surprising consequences of ion conservation in electro-osmosis over a surface charge discontinuity, J. Fluid Mech. **615**, 323 (2008).
[72] B. Gaš, M. Jaroš, V. Hruška, I. Zuskova, and M. Štedrý, PeakMaster—A freeware simulator of capillary zone electrophoresis, LC-GC Europe. **18**, 282 (2005).